Published in final edited form as:
Sci Signal. 2023 July 25; 16(795): eadd9539. doi:10.1126/scisignal.add9539.

Structure of the photoreceptor synaptic assembly of the extracellular matrix protein pikachurin with the orphan receptor GPR179

Dipak N. Patil[1,*,†], **Serena Pantalone**[2], **Yan Cao**[1], **Thibaut Laboute**[1], **Scott J. Novick**[3], **Shikha Singh**[4], **Simone Savino**[2], **Silvia Faravelli**[2], **Francesca Magnani**[2], **Patrick R. Griffin**[3], **Appu K. Singh**[5,6], **Federico Forneris**[2,7,*], **Kirill A. Martemyanov**[1,*]

[1]Department of Neuroscience, The Herbert Wertheim UF Scripps Institute for Biomedical Innovation & Technology, University of Florida, Jupiter, FL 33458, USA.

[2]The Armenise-Harvard Laboratory of Structural Biology, Department of Biology and Biotechnology, University of Pavia, Via Ferrata, 9A, I-27100 Pavia, Italy.

[3]Department of Molecular Medicine, The Herbert Wertheim UF Scripps Institute for Biomedical Innovation & Technology, University of Florida, Jupiter, FL 33458, USA.

[4]Department of Biological Sciences, Columbia University New York, NY 10027, USA.

[5]Department of Biological Sciences and Bioengineering, Indian Institute of Technology, Kanpur 208016, India.

[6]Mehta Family Centre for Engineering in Medicine, Indian Institute of Technology Kanpur, Kanpur, Uttar Pradesh 208016, India.

[7]Fondazione IRCCS Policlinico San Matteo, Pavia, Italy.

Abstract

---

[*] Corresponding author. dipakpatil@gmail.com (D.N.P.); federico.forneris@unipv.it (F.F.); kmartemyanov@ufl.edu (K.A.M.).

[†] Current address: Lilly Biotechnology Center, Eli Lilly and Company, 10290 Campus Point Dr., San Diego, CA 92121, USA.

Author contributions: D.N.P., F.F., and K.A.M. conceived of the project; D.N.P. designed and cloned the GPR179 constructs and performed preliminary screening of the constructs and generation of BacMam viruses, protein expression and production, protein purification for cryo-EM and biophysical studies, buffer optimization and preliminary screening of samples for cryo-EM study, cryo-EM data processing, model building and structural analysis, and mutagenesis and biochemical experiments; S.P. designed and cloned the pikachurin constructs and performed protein expression and production, protein purification for crystallization and biophysical studies, and collected and analyzed SEC-SAXS, MST, and SPR data. S. Singh helped with grid preparation; S.P., S. Savino, and F.F. peformed crystallization experiments and structure determination. T.L. performed functional experiments; S.J.N. performed HDX-MS analysis; P.R.G. supervised HDX-MS analysis; A.K.S. helped with cryo-EM studies; F.M. helped with biophysical experiments and data analysis. S.F. provided assistance with HEK293 cell culture for recombinant protein production; D.N.P. and K.A.M. wrote the manuscript with input from all other authors; F.F. and K.A.M. supervised the overall project implementation.

Competing interests: The authors declare that they have no competing interests.

Data and material availability: The cryo-EM density map and coordinates have been deposited in the Electron Microscopy Data bank (EMDB) and Protein Data Bank (PDB), respectively, with accession codes EMD-27121 and 8D1B for the GPR179 ECD–pikachurin LG3 complex. Coordinates and structure factors have been deposited in PDB with accession codes 7ZCB and 7ZC9 for the N- and C-terminal domains of pikachurin; SEC-SAXS data for the pikachurin domains have been deposited in the SASBDB with accession codes SASDN78 (pikachurin FN3 I-II), SASDN88 (pikachurin EGF-LG3 fragment), and SASDN68 (pikachurin LG3 domain). Raw HDX-MS data are deposited at: https://doi.org/10.6084/m9.figshare.23635530. All plasmids and viruses generated during this study are freely available upon request. All data needed to evaluate the conclusions in the paper are present in the paper or the Supplementary Materials.

Precise synapse formation is essential for normal functioning of the nervous system. Retinal photoreceptors establish selective contacts with bipolar cells, aligning the neurotransmitter release apparatus with postsynaptic signaling cascades. This involves trans-synaptic assembly between the dystroglycan-dystrophin complex on the photoreceptor and the orphan receptor GPR179 on the bipolar cell, which is mediated by the extracellular matrix protein pikachurin (also known as EGFLAM). This complex plays a critical role in the synaptic organization of photoreceptors and signal transmission, and mutations affecting its components cause blinding disorders in humans. Here, we investigated the structural organization and molecular mechanisms by which pikachurin orchestrates trans-synaptic assembly and solved structures of the human pikachurin domains by X-ray crystallography and of the GPR179-pikachurin complex by single-particle, cryo–electron microscopy (cryo-EM). The structures reveal molecular recognition principles of pikachurin by the Cache domains of GPR179 and show how the interaction is involved in the trans-synaptic alignment of the signaling machinery. Together, these data provide a structural basis for understanding the synaptic organization of photoreceptors and ocular pathology.

Introduction

In vertebrates, vision begins when light excites rod and cone photoreceptors, which hyperpolarize in response (1). The signal is then relayed to other neurons in the retina for processing and ultimately transmitted to the brain to generate an actionable neural representation of the sense (2, 3). This process crucially hinges upon the integration of photoreceptors into the neural circuitry of the retina. For this, photoreceptors form synaptic contacts with their downstream neuronal partners, the bipolar cells (BCs). In particular, photoreceptors connect with the ON-type of BC (ON-BC), forming a specialized metabotropic synapse (4-6). Failure to establish synapses with the ON-BC because of either functional or structural deficits results in night blindness accompanied by a range of visual impairments in humans (5, 7).

There has been tremendous progress made in identifying the players involved in synaptic connectivity and the transduction of signals at photoreceptor synapses (5, 8). Pre-synaptically, a crucial role in this process is played by the synaptic release apparatus of photoreceptors that controls exocytosis of the neurotransmitter glutamate (9, 10). Accordingly, on the postsynaptic ON-BC neurons, elements of the signaling cascades that respond to glutamate are essentially involved. These include the glutamate receptor mGluR6, the effector ion channel TRPM1, and a GTPase-activating protein (GAP) complex that controls mGluR6-TRPM1 coupling and involves the poorly understood orphan receptor GPR179 (5, 11-13). Furthermore, studies also identified several cell adhesion molecules that control the synaptic connectivity of photoreceptors by interacting with the signaling components in photoreceptors or ON-BCs (5, 14). One of the first identified elements with a crucial role in shaping photoreceptor contacts and signal transduction is the Agrin-like extracellular matrix protein EGFLAM, generically called pikachurin (15, 16). Research on Pikachurin showed that it forms a transsynaptic bridge that interacts with both pre-synaptic elements through its direct binding to the photoreceptor dystroglycan complex (DGC) and postsynaptically with the GPR179-GAP complex (Fig. 1A) (16, 17). Loss of pikachurin in mice results in disruption of photoreceptor synaptic organization and synaptic transmission, recapitulating the blinding phenotype of disease-causing mutations in either DGC or GPR179 in human patients and mouse models (15, 16, 18). However, the mechanisms by which pikachurin exerts its effects are incompletely understood and no structural information is available for it, let alone any transsynaptic complexes at photoreceptor synapses. Here, we used a combination of X-ray crystallography and single-particle, cryo–electron microscopy (cryo-EM) to determine the high-resolution structures of distal modules of pikachurin alone and in combination with the orphan receptor GPR179. Our results reveal how transsynaptic complexes are assembled at photoreceptor synapses and provide a mechanistic basis for understanding the role of the extracellular matrix in aligning neurotransmitter signaling cascades.

Results

Overall structural organization of pikachurin alone and in complex GPR179

We used a combination of X-ray crystallography, small-angle X-ray scattering (SAXS), and cryo-EM to obtain structures of pikachurin domains and pikachurin in a complex with the orphan receptor, GPR179. First, we deconstructed pikachurin into its domain modules, including those involved in the interaction with GPR179 (Fig. 1B). We determined high-resolution X-ray crystal structures of fibronectin type III (FN3) domains I and II and the laminin-like globular domain (LG) at resolutions of 2.5 and 2.1 Å, respectively (Fig. 1B, figs. S1 and S2, table S1).

The structure of the N-terminal FN3 domains of pikachurin display a typical β-sandwich fold of FN3, comprising seven strands in which a three-stranded antiparallel β-sheet is packed onto a four-stranded antiparallel β-sheet (Fig. 1B). Furthermore, the FN3 domains are arranged in tandem, adopting a distinct bent conformation. The bent FN3 tandem is stabilized by a 3_{10} helix in the FN3 connecting loop and a disulfide bridge between Cys^{139} of the connecting loop and Cys^{48} of FN3-I, providing rigidity to the FN3 domains. Additionally, the FN3 tandem is further stabilized by glycosylation at Asn^{47}, which occupies the inner side of the curvature (fig. S1A). To understand the oligomeric state and arrangement of the FN3 domains in solution, we used size-exclusion chromatography coupled to small-angle X-ray scattering (SEC-SAXS). These solution studies showed that the FN3 tandem is monomeric (fig. S1B and table S2) and highlighted its limited interdomain conformational freedom. Structural superposition of FN3-I onto FN3-II showed that their overall folds are similar, despite having a low sequence identity (~25%) and the presence of glycosylation site only in FN3-I (fig. S1, C and D). Structural comparison with tandem FN3 domains from other proteins showed that the FN3 assembly of pikachurin maintains the typical FN3 fold but possesses distinctive features that include a unique curvature, a connecting loop incorporating a 3_{10} helix, a disulfide bridge, and a glycosylation site (fig. S1C).

The structure of the LG3 domain of pikachurin adopts the characteristic β-jellyroll fold of an LG domain, comprising fifteen β-strands (Fig. 1B). The upper leaflet contains a seven-stranded antiparallel β-sheet, which is sandwiched by the lower leaflet formed by an eight-stranded antiparallel β-sheet. It also contains two α-helices, a single disulfide bridge (Cys^{987} to Cys^{1014}), and a glycosylation site (fig. S2A). Structural comparison with LG3 domains from other proteins revealed that the LG3 domain of pikachurin has several unique features, including a distinctly long H1 helix and a unique glycosylation site (fig. S2B). However, despite having low sequence similarity with other LG3 domains, that of pikachurin maintains a conserved Ca^{2+}-binding site and a disulfide bridge (fig. S2C). Moreover, our SEC-SAXS experiments showed that the LG3 domain of pikachurin is monomeric in solution (fig. S2D, table S2).

To visualize the transsynaptic signaling complex formed between the ECD of GPR179 and pikachurin, we determined the structure of the EGF3-LG3 tandem module of pikachurin complexed with GPR179 by cryo-EM at a resolution of 4.1 Å (figs. S3 and S4, table S3). We observed density for all of the structural elements, including the ECD and the transmembrane (TM) domain of GPR179, as well as the LG3 and EGF3 domains of pikachurin (Fig. 2A). However, for model building, we only used regions with well-resolved densities, and we excluded the TM domain, a part of the GPR179 ECD, and the EGF3 domain of pikachurin with lower interpretation confidence. Focused refinement of the GPR179 ECD–pikachurin complex further improved the quality of the cryo-EM density (Fig. 2B), enabling the precise orientation of the LG3 domains of pikachurin and the assignment of secondary structures with a resolution of 3.5 Å (figs. S3 and S4). Overall, the structure of the complex reveals two molecules of pikachurin facing each other in an opposite orientation while bound at the apex of the dimeric ECDs of the GPR179 homodimer (Fig. 2B). The LG3 domain of pikachurin directly engages GPR179, whereas the EGF3 domain is not directly involved in the interaction. GPR179 forms a homodimeric assembly with its protomers interacting through the ECD and the TM regions. Each GPR179 subunit is composed of an ECD and a TM domain connected by a flexible stalk domain. The density at the stalk and TM region of protomers were not well-resolved, limiting the analysis to their overall organization. The dimeric assembly of the TM domain suggests that dimerization is facilitated by one TM helix from each protomer, possibly a TM4-to-TM4 arrangement, based on fitting of the TM domain model from AlphaFold (fig. S4, H and I); however, the assignment of correct TM helices is limited due to the poor, discontinuous density at the TM region.

Distinct architecture of the ECD of GPR179

Analysis of the ECD regions of GPR179 shows that it features an N-terminal α-helical region, a central globular domain, and a C-terminal stalk region (Fig. 3A and fig. S5A). The globular domain shows a structural fold characteristic of Cache (CAlcium channels and CHEmotaxis receptors) domains present in bacterial chemoreceptors, auxiliary subunits of calcium channels, and also identified in a related orphan receptor, GPR158 (Fig. 3B, fig. S5, B and C) (19). The Cache domain of GPR179 is composed of six antiparallel β-sheets supported by two α-helices from the backside and several distinctive features not seen in other Cache domains: a lever-like long loop (β3β4 loop) that harbors a β-hairpin (β3'-β3'') and a 3_{10} helix (Fig. 3B). The density of the long loop was not uniformly well-resolved; however, the presence of distinct secondary structural elements (the β-hairpin and a 3_{10} helix) enabled it to be positioned (fig. S5B). The α2 helix features an extension (α2') that twists towards the apex of the domain and transitions into the loop that connects the α1 and α2 helices. The curved β-sheets are stabilized from the backside by hydrophobic interactions with the α1 and α2 helices, whereas the sheet core forms an acidic pocket in a position equivalent to the diverse ligand-binding pockets found in other Cache domains (fig. S5, C and D). A part of the "lever-like" flexible loop was not modeled due to poor density; however, it is seemingly positioned over the top of the putative ligand-binding pocket, similarly to helix α3 in other Cache domains (fig. S5B) and thus likely participates in capping the pocket from the top of the cavity, restricting the pocket size and its accessibility. Furthermore, the lever loop contains acidic residues, presumably extending the acidic environment of the pocket and possibly contributing to ligand interaction selectivity (fig. S5E).

The Cache domains of GPR179 dimerize to form a distinct supramolecular structure with core β-sheets from each protomer assembling at the outer side generating a β-barrel–like fold that entraps individual Cache domain helices inside the central pore (Fig. 3C and fig. S5F). At the same time, the core β-sheets are not directly involved in forming the dimeric interface. The α1 and α2 helices of the Cache domains cross each other to generate a four-helix bundle involving an extensive network of interactions. This bundle is lodged inside the β-barrel stabilizing the interface (fig. S5, G and H). The α2' helices from both Cache domains are positioned at the top of the β-barrel, capping it perpendicularly. One of the most prominent features of the dimeric interface is the involvement of a distinct β-hairpin that wraps the α-helices from both sides, filling the space between the core β-sheets of the Cache domains (Fig. 3C). The β-hairpin further extends the dimeric interface by interacting with the α2 helix and β3 sheet of another Cache domain (Fig. 3D and fig S6A).

The N terminus of the Cache domain is connected to the N-terminal domain (NTD) of GPR179, whereas the C terminus is connected to the stalk region. The densities of both regions were not well-resolved. The NTD is composed of two helices, whereas the stalk region contains flexible loops and has ten cysteines that may engage in intradomain disulfide bridges; however, poor density in this region limited confident model building (fig. S6, B and C). Moreover, the ECD contains a disulfide bond formed between Cys^{76} of the NTD-Cache loop and Cys^{236} of the Cache domain β4β5 loop (fig. S6B). The ECD is connected to the TM domain through the stalk region. To gain further insights into the conformational dynamics of GPR179, we performed HDX-MS analysis. These measurements showed high deuterium exchange at the lever-like loop of the Cache domain and at the stalk region of ECD, indicating conformational flexibility at these regions (fig. S7).

Overall, the ECD of GPR179 forms a distinct module not typically found in GPCRs. Whereas it resembles the architecture of the extracellular region of its closest homolog GPR158, the two ECDs are relatively distinct, which is underscored by their limited sequence similarity (42% sequence identity) (fig. S8) and the high degree of deviation upon structural alignment (RMSD values ranging from 2.2 to 3.7Å) (fig. S9A). There are several notable distinct features of the GPR179 ECD. First, the NTD region of GPR179 is composed of two helices, in contrast to the three that are present in GPR158, which have a distinct arrangement (fig. S9B). The first helix of the GPR179 NTD is longer and less conserved (fig. S8). The loop that connects the NTD with the Cache domain is shorter in GPR179 than that in GPR158, variable, and adopts a different conformation. Second, as noted earlier, the Cache domain of GPR179 features a distinct lever-like loop that is absent from GPR158 (fig. S9C). This loop is involved in both dimerization and organization of the putative ligand-binding pocket and could play a critical role in ligand recognition and selectivity. Third, the putative ligand-binding pocket of GPR179 also has notable differences from the corresponding pocket in GPR158. The pocket in GPR179 has an acidic surface potential unlike the amphipathic pocket in GPR158 and the two receptors have prominent differences in their putative ligand-interacting residues (fig. S9D). Fourth, the stalk regions of GPR158 and GPR179 contain flexible loops, reflecting their dynamic nature but which are not conserved among the two receptors (fig. S8). Despite the distinct features of the GPR179 ECD, its overall architecture, including the ordering of the domains, the presence of the Cache domain, and the conservation of cysteine positions in the ECD and dimerization, resembles that of GPR158. This suggests that both receptors share common signaling principles but that they can nevertheless deviate substantially in regulatory mechanisms and in the ligands that they recognize.

Principles of pikachurin recognition by GPR179

The structure of the pikachurin-GPR179 complex showed that the two LG3 domains of pikachurin are bound to the GPR179 homodimer at the apex of each Cache domain, involving the α2' helix and the β1β2, β5β6, and β-hairpin loops (Fig. 2B, Fig. 4A, fig. S10, A and B). From the pikachurin side, the binding is mediated by the lower leaflet of a β-jellyroll fold positioned perpendicularly on the top α2' helix of the Cache domain. The LG3 domains face each other in reverse orientation. Each LG3 domain interacts with one Cache domain protomer in the same way. The LG3 Asn^{917} glycosylation site is distant from the GPR179-LG3 contact interfaces (Fig. 4A). Together, this arrangement forms a tetrameric assembly with two LG3 domains engaging dimeric Cache domains forming an extensive binding interface (Fig. 4A).

The interaction network of Cache domains engaging individual LG3 domain is extensive and can be divided into three sites (Fig. 4B). Binding site I mostly involves the α2' helix of the Cache domain covering from the central part to one corner of the lower leaflet of the β-jellyroll fold, with a β-hairpin loop stabilizing from another corner. Both the α2' helix and β-hairpin that contribute to GPR179 dimerization at the ECD form a substantial binding interface through an extensive network of hydrophilic interactions with residues of β-sheets S8, S9, and loop S9S10 of pikachurin (fig. S10C). Note that two acidic residues of the α2' helix are engaged in ionic interactions with basic residues of the β-sheets. Asp^{117} and Glu^{120} of the α2' helix form ionic bonds with Lys^{938} of S9 and Lys^{929} of S8, respectively, whereas Lys^{213} of the β-hairpin loop engages in an ionic pairing with Asp^{943} and hydrogen bonding with Tyr^{944} of the S9S10 loop to stabilize the interaction (fig. S10C). Another prominent binding interface is formed by site II, which stabilizes the complex and comprises all loops, namely the β5β6 loop of the Cache domain and loops S8S9 and S10S11 of the LG3 domain. Site II may be stabilized by the formation of two ionic pairs between the interface residues present in proximity to each other (fig. S10D). Finally, site III, in the opposite corner from β-hairpin loop of site I, is composed of the β1β2 loop of the Cache domain and the S12S13 and H1S3 loops of LG3 domain, which stabilize the interface through hydrophilic interactions (fig. S10E).

In the context of pikachurin-GPR179 binding, the α2' helix and β-hairpin at the dimeric interface of the GPR179 ECDs are both engaged in pikachurin binding, suggesting that docking of pikachurin molecules involves the interaction interface of the GPR179 protomers. This is also evident from electrostatic surface potential analysis of the GPR179 ECD, which shows an overall negative charge at the binding interface, providing a favorable complementary surface for docking positively charged pikachurin LG3 domains (Fig. 4C). Overall, the GPR179-pikachurin complex is strongly stabilized by an extensive network of interactions, which are predominantly hydrophilic and ionic. This is further supported by our SPR and MST analysis, showing higher binding affinities (K_D values of 290 and 175 nM, respectively) between the GPR179 ECD and the pikachurin EGF3-LG3 domain (fig. S11).

To understand why only the terminal EGF3-LG3 module is capable of binding to GPR179 despite the presence of two other similar EGF-LG tandems in the pikachurin molecule (17), we compared the experimentally observed structure of LG3 with the structures of LG1 and LG2 as predicted by AlphaFold. Whereas all LG modules share a similar fold, we note substantial differences in the loops, including those involved in the interaction with GPR179 (fig. S12A). Most importantly, most of the binding determinants that are crucial for GPR179 binding are not conserved in LG1 and LG2, especially at sheets S8, S9, and S10, and at loops S8S9 and S9S10 (fig. S12B). Moreover, the overall surface electrostatic charge at the corresponding binding interface differs between LG1 and LG2 and is predicted to be unfavorable for GPR179 binding (fig. S12C). All of these differences result in the LG3 domain being distinctly suitable for GPR179 binding, whereas other modules possibly specialize in interactions with other binding partners, including the DGC complex (16), to form a supramolecular assembly.

Furthermore, binding to GPR179 brings the two LG3 domains of pikachurin close together, and their orientation and positioning is likely shaped by the interaction of the respective LG3 protomers with the Cache domains of GPR179. Because Cache domains are tightly integrated together by extensive interactions, binding of the LG3 domains of pikachurin likely occurs in the context of GPR179 dimerization. Consistent with this speculation, our SEC-SAXS studies showed that, similar to LG3, the EGF3-LG3 construct of pikachurin is also monomeric in solution (fig. S13A, table S2).

To address a question about the conformational consequences of GPR179-pikachurin interactions, we compared the crystal structure of LG3 domain in the apo form with its cryo-EM–derived structure when bound to GPR179. We detected re-organization of the loops at the lower leaflet of the β-jellyroll fold upon GPR179 binding (RMSD value of 1.08Å). Loops S7S8, S8S9, S10S11, and S12S13 re-arrange to form contacts with GPR179 (fig. S13B). Extracellular interactions of some GPCRs can alter their signaling (20). Therefore, we next tested whether pikachurin binding induced an alteration in GPR179 function. For this, we used BRET-based reporter assays to study the effect of pikachurin on the GAP activity of the GPR179-RGS7 complex. These experiments showed that the addition of pikachurin did not influence the kinetics of deactivation of $G\alpha_o$ (fig. S14), a substrate regulated by the GPR179-RGS7 complex in ON-BC neurons to enable synaptic transmission of the light signal. Although the absence of a ligand for GPR179 that can serve as a positive control limits the interpretation of these results, they are consistent with the observation that pikachurin does not interact with the putative orthosteric pocket in the Cache domains of GPR179.

Discussion

Here, we present structures of the retina-specific ECM protein pikachurin and show how it binds to the client receptor that it controls: GPR179, an orphan class C GPCR. Interactions between GPCRs and extracellular proteins is an emerging theme in the field (21). Classical models of GPCRs nearly exclusively ascribe ligand-binding function to the large extracellular domains particularly prominently present in class C receptors. However, other evidence suggests that the ECDs of class C GPCRs are also engaged in interactions with cell adhesion molecules that control their functional activity and localization (22-25); however, a structural basis for these interactions is lacking.

GPR179 is a noncanonical receptor that instead of activating heterotrimeric G proteins recruits the RGS protein complex, which signals by deactivating its substrate Gα_o, an event that leads to the opening of the ion channel TRPM1, thereby depolarizing the cell (12, 13, 26). This unusual assembly requires positioning of the GPR179 complex precisely at the synaptic sites, which is achieved through its transsynaptic interactions involving the extracellular matrix protein pikachurin (17). Our work reveals how pikachurin may recruit GPR179 complex to the synaptic sites at the atomic level. Pikachurin uses its distal LG domain to engage a distinct surface of the presumptive ligand-binding domain of GPR179 called the Cache domain. This interaction occurs at a site distinct from the putative pocket in the Cache domain, thereby likely not impeding ligand interactions. Consistent with this observation, we observed that pikachurin binding failed to influence GPR179 activity, indicating that it is unlikely to serve as a bona fide ligand. Instead, pikachurin seems to be an auxiliary subunit of GPR179, potentially guiding its synaptic insertion and conformational state for optimal positioning of the intracellular RGS complex. We also determined the structure of the FN3 domain of pikachurin, which is not directly involved in the interaction with GPR179. We speculate that it likely plays a structural role in ensuring the proper orientation of the pikachurin molecule in the synaptic cleft or that it might be involved in the recruitment of additional binding partners.

Our findings also reveal the presence of the Cache domain in GPR179, an unusual feature not commonly observed in GPCRs. The only other receptor known to contain a Cache domain is GPR158, with which GPR179 shows some homology (19). The Cache domain of GPR179 features a clearly identifiable pocket well that is suited for binding to small molecules. This pocket is analogous to the ligand-binding pockets in the Cache domains of bacterial chemoreceptors (27), suggesting that GPR179 may also use it to detect small-molecule ligands. Indeed, this pocket in GPR158 has been recently identified as a binding site for its ligand, glycine (28). However, the pocket in GPR179 appears to be quite distinct from that seen in GPR158, suggesting that its ligand is also likely different. The interaction of the Cache domain with the LG domain that we report here suggests that Cache-LG binding may be a general phenomenon.

Finally, our findings offer potential insights into the molecular mechanisms underlying the pathology of Congenital Stationary Night Blindness (CSNB), a blinding disorder associated with defects in signal transmission from rod photoreceptors to bipolar cells in the retina (7). Mutations in GPR179 have a causal role in CSNB (12, 13). Synaptic localization of GPR179 is controlled by pikachurin, and loss of pikachurin similarly impairs the synaptic communication between rods and bipolar cells (16, 17). Note that two mutations of GPR179, D126H and Y220C, are located in the Cache domain. Asp^{126} is present at the α2' helix that participates in the GPR179 ECD dimeric interface, as well as the binding interface of pikachurin, whereas Tyr^{220} is located on β-hairpin sheet β3" of the β3β4 loop and is not directly involved in binding to pikachurin (Fig. 5A). Both the D126H and Y220C mutations may disrupt the structural integrity of the GPR179 homodimeric assembly by destabilizing the Cache domain dimeric interface either directly (D126H) or by hampering core assembly by breaking the π-π interaction in the β-hairpin loop (Y220C) (Fig. 5B). These deficiencies could explain the surface trafficking defects that have been observed for the Y220C mutant (29). Our model suggests that pikachurin-GPR179 binding may be perturbed by CSNB-associated mutations. However, directly investigating this experimentally will be challenging due to the mutually co-stabilizing nature of the complex and the associated effects of the mutations on the cell-surface trafficking of GPR179, pikachurin, or both. In general, we envision that the availability of the high-resolution structural information of the pikachurin-GPR179 complex will facilitate studies of the molecular etiology of human blinding disorders.

Materials and Methods

Culture and transfection of clonal cell lines

For GPR179 (1-740) production, HEK293 GnTI^{-} cells (ATCC, CRL-3022) were cultured at 37°C in 8% CO_2 using FreeStyle 293 Expression Medium (Life Technologies) supplemented with 2% fetal bovine serum (FBS). FN3 I-II (25-237), EGF3-LG3 (784-1017), LG3 (831-1017), and GPR179 ECD (UniProt entry Q6PRD1, 26-380) were produced in HEK293F cells. For functional studies, HEK293FT cells (ThermoFisher Scientific, R70007) were cultured in Dulbecco's modified Eagle's medium (DMEM) supplemented with 10% FBS (v/v), minimum Eagle's medium non-essential amino acids, 1 mM sodium pyruvate, and antibiotics (100 units/ml penicillin and 100 mg/ml streptomycin) at 37°C in a humidified incubator with 5% CO_2. HEK293FT Cells were transiently transfected with Metafectene Pro (Biontex, Germany) in 96-well plates according to the manufacturer's instructions.

Generation of human GPR179 BacMam virus

We generated a construct encoding human GPR179 with a C-terminal truncation. The construct was modified to include a C-terminal 3C protease cleavage, eGFP, the Flag tag, and a 10× histidine tag. We subcloned the construct into modified pEG BacMam vector (30). The baculovirus containing GPR179 was generated and amplified in Sf9 cells (ThermoFisher Scientific, 11496015).

GPR179 expression and purification

For protein production, HEK293 GnTI⁻ cells were cultured at a density of 3.0 × 10^6 cells/ml and infected with GPR179 high titer P3 BacMam viruses. To enhance the expression, 10 mM sodium butyrate was added to the culture 12 hours after infection. The culture was further incubated for 48 hours at 30°C and the cells were harvested by centrifugation and stored at −80 °C. To purify GPR179, the cells were suspended in 20 mM Tris (pH 8.0), 250 mM NaCl, 10% glycerol, 0.5 mM PMSF and complete Protease Inhibitor Cocktail tablets (Roche). To solubilize cell membranes, 1% (w/v) lauryl maltose neopentyl glycol (LMNG, Anatrace) supplemented with 0.2% (w/v) cholesteryl hemisuccinate (CHS, Anatrace) was added to the suspended cells. After the cells were disrupted with a sonicator, cell membranes were solubilized for 2 hours at 4°C. The insoluble matter was removed by centrifugation, and the clarified supernatant was incubated with M2 anti-Flag affinity resin for 1 hour with gentle rotation. The unbound proteins were washed with stepwise gradient (0.1 to 0.005%) of LMNG. Finally, GPR179 was eluted with 20 mM Tris (pH 8.0), 100 mM NaCl, 0.005% LMNG, 0.001% CHS. and 0.2 mg/ml Flag peptide. The eluted GPR179 fractions were collected and subjected to 3C protease cleavage to remove eGFP and the affinity purification tags. Uncleaved proteins were removed by incubation with M2 anti-Flag affinity resin. The cleaved protein was collected as flow-through and concentrated with an Amicon Ultra Centrifugal Filter (MWCO 100 kDa). GPR179 was further purified with a Superose 6 increase column (GE Healthcare) pre-equilibrated with 20 mM Tris (pH 8.0), 100 mM NaCl, 0.005% LMNG, and 0.001% CHS. The peak fractions were pooled and concentrated to 0.2 mg/mL for the cryo-EM study.

Expression and purification of pikachurin constructs

The coding sequences for pikachurin constructs (referred to UniProt entry Q63HQ2) encompassing FN3 I to II (amino acid residues 25 to 237), EGF3-LG3 (residues 784 to 1017), and LG3 (residues 831 and 1017), and the GPR179 ECD (UniProt entry Q6PRD1, residues 26 to 380) were subcloned into the pUPE.06.03 and pUPE.106.08 expression vectors (U-protein Express BV), to provide secreted, noncleavable, and Tobacco Etch Virus (TEV) protease–cleavable N-terminal, His-tagged variants of the recombinant proteins. Recombinant expression in HEK293F cells was performed for all constructs as described previously (31). Briefly, HEK293F cells (Life Technologies) in suspension were transfected at a confluence of 1 x 10^6 cells/ml with 1 μg of plasmid DNA and 3 μg of linear polyethyleneimine (PEI; Polysciences). Cells were harvested 6 days after transfection by centrifugation for 15 minutes at 1000*g*. The clarified medium was filtered with a 0.8-mm Minisart GF syringe filter (Sartorius) and the pH was adjusted to 8.0 before being subjected to immobilized metal ion affinity chromatography exploiting the affinity of the 6xHis tag for a HisTrap Excel 5 mL (GE Healthcare) affinity column. Recombinant samples carrying removable His-tags were then subjected to TEV cleavage, which was followed by reverse IMAC purification. All samples underwent further purification on a Superdex 75 Increase 10/300 GL (GE Healthcare) equilibrated in 25 mM HEPES/NaOH, 200 mM NaCl (pH 8.0), to obtain homogenous samples. Peak fractions containing the protein of interest were pooled, concentrated, flash-frozen in liquid nitrogen, and stored at −80 °C until usage.

Crystallization, data collection, structure determination, and refinement

pikachurin crystallization experiments were performed with the hanging-drop vapor-diffusion method protocols. The N-terminal pikachurin FN3 I-II construct was crystallized at 20°C by mixing 0.5 μl of pure protein concentrated at 8 mg/ml with 0.5 μl of reservoir solution composed of 18% polyethylene glycol (PEG) 3350 and 180 mM sodium bromide. The C-terminal pikachurin LG3 construct was crystallized at 20°C by mixing 0.5 μl of pure protein concentrated at 12 mg/ml with 0.5 μl of reservoir solutions composed of 1.5 to 2.0 M ammonium sulfate, 100 mM sodium acetate (pH 4.6). Crystals were cryo-protected with the mother liquor supplemented with 20% glycerol, harvested with MicroMounts Loops (Mitegen), flash-cooled, and stored in liquid nitrogen prior to data acquisition. X-ray diffraction data were collected at the European Synchrotron Radiation Facility (ESRF), Grenoble. Data were indexed and integrated with *XDS* (32) and scaled with *Aimless* (33). Data collection statistics are summarized in table S1. Both structures were solved by molecular replacement with *PHASER* (34) using the structure of the C-terminal extended domain of human myomesin-1 [PDB ID: 5FM4, (35)] and the structure of the LG3 domain of human perlecan [PDB ID: 3SH4, (36)] as search models for the N- and C- terminal pikachurin constructs, respectively. Initial model building was performed by extensive usage of *phenix.autobuild* (37) and *ARP/wARP* (38), followed by iterative cycles of manual rebuilding in *COOT* (39) and automated refinement with *phenix.refine* (40). Model validation was performed with the validation tools available at the Protein Data Bank (41). Refinement statistics for the final models are reported in table S1.

Cryo-EM sample preparation and data acquisition

For complex formation, GPR179 was incubated at equimolar concentrations with pikachurin EGF3-LG3 at 4°C for 30 min. The complex was centrifuged before grid preparation. Three microliters of GPR179-pikachurin complex were applied to freshly glow-discharged 300 mesh Gold grids (UltraAufoil R1.2/1.3) inside a FEI Vitrobot Mark IV (Thermo Fischer Scientific) that was set at 4°C and 100% humidity. A blot force of 2, blot time of 3 s, and wait time of 20 s was used before excess sample was blotted, and the grids were plunge-frozen in liquid ethane. Cryo-EM images of the GPR179-pikachurin complex were acquired on a 300 kV Titan Krios equipped with a Gatan K3 Summit direct electron detection (DED) camera (Gatan) and a post-column GIF Quantum energy filter operating in counting mode at a magnification of 105,000, giving a nominal pixel size of 0.855 Å. A total of 6,538 movies were collected with a defocus range of −1.3 to −2.1 μm. A total dose of 40 $e^{-}Å^{-2}$ was attained with a dose rate of ~11.81 e^{-}/s/phys Pixel per frame across 40 frames for a 2.5-s total exposure time.

Image processing and 3D reconstruction

The dataset was processed with RELION (42), CryoSPARC (43), or both (fig. S3 and table S1). Movies were motion-corrected for beam-induced motion in RELION with MotionCor2 (44). The contrast transfer function (CTF) estimation was performed in CryoSPARC with the patch CTF estimation tool on motion-corrected images. Unsuitable micrographs were filtered out with the exposure curation module of CryoSPARC with a CTF fit <6, resulting in 5,186 micrographs that were selected for further processing. We used the CryoSPARC

TOPAZ program for particle selection and extraction (45), which resulted in a total of 1,194,494 particles. Selected particles were subjected to ab-initio reconstruction, which was followed by heterogenous and homogenous and non-uniform (NU) refinement. A set of 249,466 particles was re-extracted after NU refinement to further improve the density at the TM region and was further subjected to ab-initio reconstruction. After heterogenous refinement, a set of 139,675 particles was chosen and subjected to NU refinement. To further improve the quality of the map, we performed 2D classification to remove junk particles, and selected particles were subjected to ab-initio reconstruction into two classes. After heterogenous refinement, a set of 67,145 particles was subjected to NU refinement, resulting in a final resolution of ~4.1Å. We then performed local refinements with a mask on the ECD-like and TM domains, individually, resulting in a resolution of 3.57 Å for ECD-pikachurin, whereas the map did not improve for the TM domain. The reported resolutions of the final maps were estimated with the gold-standard Fourier shell correlation (GSFSC) in CryoSPARC (43). The local resolution predictions were calculated by local resolution estimation with CryoSPARC, with the resolution range estimated with the FSC = 0.143 criterion (42). EM density visualization was performed in UCSF Chimera (46).

Model building and refinement

We used the GPR179 ECD and pikachurin EGF3 models predicted by AlphaFold to initially dock into the cryo-EM map with UCSF Chimera (46). Two protomers of each model were fitted onto the cryo-EM density and then were manually adjusted, built, and real space–refined in COOT (47). The local resolution in the TMD was relatively low, so the model could not be built confidently, assigning each TM helices. We fitted the TM domain and its dimerization based on the overall organization guided by the position of ECL2 and a loop connecting to TM1; however, densities for the TM helices were poorly resolved and dis-continuous, which limited our analysis broadly to the overall TM organization. For building atomic model of LG3, we further used the crystal structure of LG3. Both full-length and local refined ECD-pikachurin models were subjected to iterative manual building in COOT, which was followed by real space–refinement in PHENIX against the corresponding sharpened map using global minimization, local rotamer fitting, and restrained group ADP refinement. All of the resulting models were refined against both the un-filtered half maps and full maps using the real-space refinement algorithm and were subsequently validated with comprehensive validation (cryo-EM) in PHENIX (48). Structures were visualized and figures were prepared in UCSF Chimera (46), ChimeraX (49), and PyMOL (https://pymol.org/2/). The data collection and refinement statistics are listed in table S3.

Size-exclusion chromatography coupled to small angle X-ray scattering (SEC-SAXS)

SEC-SAXS experiments with recombinant pikachurin Fn3 1-2, EGF3-LG3, and LG3 constructs were performed at the B21 beamline of Diamond Synchrotron Light Source (DLS, Didcot, UK). Fifty microliters of each sample at different concentrations (ranging from 0.5 to 2.5 mg/ml) were injected into a Superdex 75 3.2/300 (GE Healthcare) column pre-equilibrated in 25 mM HEPES/NaOH, 200 mM NaCl (pH 8). Data collection parameters are listed in table S2. SEC-SAXS data were analyzed with the *ATSAS* suite. In particular, scattering frames corresponding to samples were selected, averaged, and subtracted from averaged buffer frames using *CHROMIXS* (50). The buffer-subtracted, 1D scattering curves were then processed with *PRIMUS* (51) to compute the radii of gyration (R_g), and obtain molecular mass estimates; the pair distribution function (*P(r)*) and the maximum particle dimension (D_{max}) were estimated from the scattering data with the algorithm available in *GNOM* (52). Ab-initio sphere models were generated through repeated iterations with *GASBOR* (53), by providing the software with *P(r)* (53) functions derived from experimental data and the number of residues defining each pikachurin construct. Ten independent, ab initio *GASBOR* runs were performed and subjected to a similarity analysis with *SUPCOMB* and *DAMSEL* from *ATSAS* (54), which enabled selection of a representative individual model based on normalized spatial discrepancy. Superpositions of the ab initio sphere models with atomic structures were obtained with the *SUPALM* tool of the *SASpy* PyMol plugin (55).

Microscale thermophoresis (MST)

The GPR179 ECD construct devoid of the His-tag was labeled with the RED-NHS dye of the MST Labeling Kit (NanoTemper) according to the manufacturer's instructions, reaching a final concentration of 6 µM conjugated protein. Both the labeled GPR179 ECD (ligand) and the recombinant pikachurin EGF3-LG3 (analyte) were diluted with 25 mM HEPES/NaOH, 200 mM NaCl (pH 8), supplemented with 0.05% Tween-20 to avoid non-specific aggregation/adsorption and autofluorescence. Labeled GPR179 ECD was used as target in MST measurements at a final concentration of 200 nM. Experiments were performed with a Monolith NT.115 (NanoTemper) instrument set at 25°C and with standard-treated capillaries (NanoTemper). An MST protocol composed of pretest, binding check, and binding affinity experiments was followed. Experimental settings were as follows: excitation power: 20%; MST power: high; Thermostat Setpoint: 25.0°C; MST-on time: 2.5 s. In the last step, pikachurin EGF3-LG3 was used as analyte in a titration series of 16 points each, in a concentration range from 0.0014 to 47 µM. Data were analyzed with MO.Affinity Analysis software version 2.2.4 (NanoTemper) to extrapolate binding affinity constants (K_d). Graphs were generated with GraphPad Prism.

Surface-plasmon resonance (SPR)

Recombinant GPR179 ECD devoid of the His-tag was immobilized onto a carboxymethylated dextran (CM5) sensor chip (Xantec) with a solution of 200 mM 1-ethyl-3-(3-dimethylaminopropyl)carbodiide hydrochloride (EDC) in 50 mM N-hydroxysuccinamide (NHS). Excess reactive groups were blocked with 1 M ethanolamine. Experiments were performed with a Biacore T200 SPR instrument (GE Healthcare). After verifying successful immobilization through the observation of a ~600 resonance unit (RU) increase on the FC2, FC3, and FC4 experiment cells of the sensor chip, the FC1 cell was prepared with the same protocol but without adding protein sample and was therefore used as reference cell during measurements. Serial dilutions between 10 and 0.035 µM of the pikachurin EGF3-LG3 construct devoid of the His-tag were made in the PBS-P + 0.01% running buffer (GE Healthcare) and injected at a flow rate of 30 µl/min with a contact time of 60 s. At the end of each sample injection, the sensor surface was regenerated by flowing 1 M NaCl over it for 10 s. Sensorgrams were recorded at 25°C and the results were analyzed with Biacore T200 evaluation software (GE Healthcare). Graphs were generated with GraphPad Prism.

Hydrogen-deuterium exchange (HDX) detected by mass spectrometry (MS)

Differential HDX-MS experiments were conducted as previously described with a few modifications (56). The following sample-processing protocol was followed. Five microliters of a 10 μM protein complex (GPR179) were diluted into 25 μl of protein storage buffer, quenched by mixing with 25 μl of 3M urea and 1% trifluoroacetic acid. Each sample was passed through an immobilized pepsin column, and the digested peptides were captured on a C8 trap column and desalted. Peptides were separated across a C18 column with a linear gradient of 4 to 40% CH_3CN and 0.3% formic acid, with a gradient of 5 min for HDX and 1 hour for tandem MS (MS/MS). Mass spectrometric data were acquired with a Q Exactive mass spectrometer. Peptides were identified by MS/MS with an Orbitrap mass spectrometer (Q Exactive, ThermoFisher). Product ion spectra were acquired in data-dependent mode, with the top five most abundant ions selected for the product ion analysis per scan event. The MS/MS data files were submitted to Mascot (Matrix Science) for peptide identification. Peptides included in the HDX analysis peptide set had a MASCOT score >20 and the MS/MS spectra were verified by manual inspection. The MASCOT search was repeated against a decoy (reverse) sequence, and ambiguous identifications were ruled out and not included in the HDX peptide set. For HDX-MS analysis, 10 μM GPR179 was incubated with pikachurin at a 1:10 molar ratio for 1 hour at room temperature. Next, 5 μl of sample was diluted into 20 μl of D_2O buffer [20 mM Tris-HCl (pH 7.4), 150 mM NaCl, 2 mM DTT) and incubated for various times (0, 10, 60, 300, and 900 s) at 4°C. The deuterium exchange was then slowed by mixing the sample with 25 μl of cold (4°C) 3 M urea and 1% trifluoroacetic acid. Quenched samples were immediately injected into the HDX platform. Upon injection, samples were passed through an immobilized pepsin column (2 mm × 2 cm) at a rate of 200 μl/min, and the digested peptides were captured on a 2 mm × 1 cm C_8 trap column (Agilent) and desalted. Peptides were separated across a 2.1 mm × 5 cm C_{18} column (1.9 μl of Hypersil Gold, ThermoFisher) with a linear gradient of 4 to 40% CH_3CN and 0.3% formic acid, over 5 min. Sample handling, protein digestion, and peptide separation were performed at 4°C. MS data were acquired with an Orbitrap mass spectrometer (Exactive, ThermoFisher). HDX analyses were performed in triplicate, with single preparations of each protein-ligand complex. The intensity-weighted mean m/z centroid value of each peptide envelope was calculated and subsequently converted into a percentage of deuterium incorporation. This was accomplished by determining the observed averages of the undeuterated and fully deuterated spectra and using a conventional formula described previously (57). Statistical significance for the differential HDX data was determined by an unpaired *t* test for each time point, a procedure that is integrated into the HDX Workbench software (58). Corrections for back exchange were made based on an estimated 70% deuterium recovery and accounting for the known 80% deuterium content of the deuterium exchange buffer. For data rendering, the HDX data from all overlapping peptides were consolidated to individual amino acid values through a residue-averaging approach. Briefly, for each residue, the deuterium incorporation values and peptide lengths from all overlapping peptides were assembled. A weighting function was applied in which shorter peptides were weighted more heavily and longer peptides were weighted less. Each of the weighted deuterium incorporation values was then averaged to produce a single value for each amino acid. The initial two residues of each peptide, as well as prolines, were omitted from the calculations. This approach is similar to that previously described

(59). HDX analyses were performed in triplicate, with single preparations of each purified protein/complex. Statistical significance for the differential HDX data was determined by a *t* test for each time point and was integrated into the HDX Workbench software (58).

Cell-based GAP assay

The assay performed to monitor the GAP activity of RGS7 was conducted as described previously (60). Briefly, HEK293FT cells were seeded in a white, flat-bottom, 96-well plate (Greiner Bio-One) at 50,000 cells/well and transiently transfected with pcDNA3.1(+) plasmids encoding the dopamine D_2 receptor (cDNA Resource Center : #DRD0200001), RGS7 (GenBank: AY587875), $G\beta_5$ (GenBank: NM_016194), $G\alpha_{oA}$ (cDNA Resource Center : #GNA0OA0000), GPR179 (Origene : #NM_001004334), as well as masGRK3ct-Nluc, Venus-156-239-Gβ1, and Venus-1-155-Gγ2 (synthesized by GenScript). Twenty-four hours after transfection, the cells were washed with BRET buffer [Dulbecco's phosphate-buffered saline (PBS) containing 0.5 mM $MgCl_2$ and 0.1% glucose] and incubated for 5 min at 37°C with the The NanoLuc (Nluc) substrate, furimazine (Promega: #N1110) according to the manufacturer's instructions with or without the pikachurinc-LG3/EGF3-LG3 protein. To to activate or deactivate the D2 receptor, respectively, dopamine or haloperidol (100 μM each) were injected sequentially and automatically onto the cells by the plate reader (PHERAstar FSX, BMG Labtech), and dual-luminescence were measured at 475 ±30 nm and 535 ±30 nm. All measurements were performed at 37°C. The BRET signal was determined by calculating the ratio of the light emitted by Venus-Gβ1γ2 (535 nm with a 30-nm band path width) to the light emitted by masGRK3ct-Nluc (475 nm with a 30-nm band path width). The average baseline value (basal BRET ratio) recorded before agonist treatment was subtracted from the experimental BRET signal values, and the resulting difference (ΔBRET ratio) was normalized relative to the maximal ΔBRET value recorded upon agonist treatment. The rate constant ($1/\tau$) of the deactivation phases was obtained by fitting a single exponential decay curve to the traces with Graphpad Prism 9.0. No data were excluded from the analysis. The resulting values were plotted and evaluated to detect differences from the symmetric normal distribution, which was found not to be Gaussian. The Kruskal-Wallis test was used to evaluate differences across treatments, which was followed by Dunn's test for post hoc analysis.

Supplementary Material

Refer to Web version on PubMed Central for supplementary material.

Acknowledgments:

We thank R. Grassucci, Z. Zhang, and Y.-H. Kao of the Cryo-Electron Microscopy Center, Columbia University and T. Edwards and T. Fox of the NCI National Cryo-EM Facility for cryo-EM support, and the ESRF and Diamond synchrotron facilities for infrastructure provision for X-ray diffraction and SAXS experiments. We also thank D. K. Jaijyan for help with cryo-EM samples, L. Scietti for help with SPR experiments, and L. V. Viti for help in modeling of the pikachurin N-terminal crystal structure.

Funding:

This work was supported by NIH grant MH105482 (to K.A.M.) and a Velux Stiftung grant 1375 (to F.F.). This research was, in part, supported by the National Cancer Institute's National CryoEM Facility at the Frederick National Laboratory for Cancer Research under contract HSSN261200800001E, the Giovanni Armenise-Harvard

Foundation (CDA 2013 to F.F.), and the Dipartimenti di Eccellenza Program 2018-2022 (to F.F.). A.K.S. is a DBT-IYBA and Ramalingaswamy DBT fellow and is supported by SERB-SRG funding agency (SERB/SRG/2020/000266).

References and Notes

1. Burns ME, Arshavsky VY, Beyond counting photons: trials and trends in vertebrate visual transduction. Neuron 48, 387–401 (2005); published online EpubNov 3 ([PubMed: 16269358]
2. Hoon M, Okawa H, Della Santina L, Wong RO, Functional architecture of the retina: development and disease. Progress in retinal and eye research 42, 44–84 (2014); published online EpubSep (10.1016/j.preteyeres.2014.06.003). [PubMed: 24984227]
3. Sanes JR, Zipursky SL, Design principles of insect and vertebrate visual systems. Neuron 66, 15–36 (2010); published online EpubApr 15 (10.1016/j.neuron.2010.01.018). [PubMed: 20399726]
4. Morgans CW, Brown RL, Duvoisin RM, TRPM1: the endpoint of the mGluR6 signal transduction cascade in retinal ON-bipolar cells. Bioessays 32, 609–614 (2010); published online EpubJul (10.1002/bies.200900198). [PubMed: 20544736]
5. Martemyanov KA, Sampath AP, The Transduction Cascade in Retinal ON-Bipolar Cells: Signal Processing and Disease. Annu Rev Vis Sci, (2017); published online EpubJul 17 (10.1146/annurev-vision-102016-061338).
6. Vardi N, Dhingra A, in G Protein Signaling Mechanisms in the Retina, Martemyanov K, Sampath AP, Eds. (Springer, New York, 2014), vol. 3, pp. 81–98.
7. Zeitz C, Robson AG, Audo I, Congenital stationary night blindness: an analysis and update of genotype-phenotype correlations and pathogenic mechanisms. Progress in retinal and eye research 45, 58–110 (2015); published online EpubMar (10.1016/j.preteyeres.2014.09.001). [PubMed: 25307992]
8. Gregg RG, Ray TA, Hasan N, McCall MA, Peachey NS, in G Protein Signaling Mechanisms in the Retina, Martemyanov K. A. a. S., A.P., Ed. (Springer, 2014), vol. 3, pp. 67–79.
9. Mercer AJ, Thoreson WB, The dynamic architecture of photoreceptor ribbon synapses: cytoskeletal, extracellular matrix, and intramembrane proteins. Vis Neurosci 28, 453–471 (2011); published online EpubNov (10.1017/S0952523811000356). [PubMed: 22192503]
10. Pangrsic T, Singer JH, Koschak A, Voltage-Gated Calcium Channels: Key Players in Sensory Coding in the Retina and the Inner Ear. Physiological reviews 98, 2063–2096 (2018); published online EpubOct 1 (10.1152/physrev.00030.2017). [PubMed: 30067155]
11. Orlandi C, Cao Y, Martemyanov KA, Orphan receptor GPR179 forms macromolecular complexes with components of metabotropic signaling cascade in retina ON-bipolar neurons. Invest Ophthalmol Vis Sci 54, 7153–7161 (2013)10.1167/iovs.13-12907). [PubMed: 24114537]
12. Peachey NS, Ray TA, Florijn R, Rowe LB, Sjoerdsma T, Contreras-Alcantara S, Baba K, Tosini G, Pozdeyev N, Iuvone PM, Bojang P Jr., Pearring JN, Simonsz HJ, van Genderen M, Birch DG, Traboulsi EI, Dorfman A, Lopez I, Ren H, Goldberg AF, Nishina PM, Lachapelle P, McCall MA, Koenekoop RK, Bergen AA, Kamermans M, Gregg RG, GPR179 Is Required for Depolarizing Bipolar Cell Function and Is Mutated in Autosomal-Recessive Complete Congenital Stationary Night Blindness. Am J Hum Genet 90, 331–339 (2012); published online EpubFeb 10 (10.1016/j.ajhg.2011.12.006). [PubMed: 22325362]
13. Audo I, Bujakowska K, Orhan E, Poloschek CM, Defoort-Dhellemmes S, Drumare I, Kohl S, Luu TD, Lecompte O, Zrenner E, Lancelot ME, Antonio A, Germain A, Michiels C, Audier C, Letexier M, Saraiva JP, Leroy BP, Munier FL, Mohand-Said S, Lorenz B, Friedburg C, Preising M, Kellner U, Renner AB, Moskova-Doumanova V, Berger W, Wissinger B, Hamel CP, Schorderet DF, De Baere E, Sharon D, Banin E, Jacobson SG, Bonneau D, Zanlonghi X, Le Meur G, Casteels I, Koenekoop R, Long VW, Meire F, Prescott K, de Ravel T, Simmons I, Nguyen H, Dollfus H, Poch O, Leveillard T, Nguyen-Ba-Charvet K, Sahel JA, Bhattacharya SS, Zeitz C, Whole-Exome Sequencing Identifies Mutations in GPR179 Leading to Autosomal-Recessive Complete Congenital Stationary Night Blindness. Am J Hum Genet 90, 321–330 (2012); published online EpubFeb 10 (10.1016/j.ajhg.2011.12.007). [PubMed: 22325361]
14. Tummala SR, Dhingra A, Fina ME, Li JJ, Ramakrishnan H, Vardi N, Lack of mGluR6-related cascade elements leads to retrograde trans-synaptic effects on rod photoreceptor synapses via

matrix-associated proteins. Eur J Neurosci 43, 1509–1522 (2016); published online EpubJun (10.1111/ejn.13243). [PubMed: 27037829]

15. Omori Y, Araki F, Chaya T, Kajimura N, Irie S, Terada K, Muranishi Y, Tsujii T, Ueno S, Koyasu T, Tamaki Y, Kondo M, Amano S, Furukawa T, Presynaptic dystroglycan-pikachurin complex regulates the proper synaptic connection between retinal photoreceptor and bipolar cells. J Neurosci 32, 6126–6137 (2012); published online EpubMay 2 (10.1523/JNEUROSCI.0322-12.2012). [PubMed: 22553019]
16. Sato S, Omori Y, Katoh K, Kondo M, Kanagawa M, Miyata K, Funabiki K, Koyasu T, Kajimura N, Miyoshi T, Sawai H, Kobayashi K, Tani A, Toda T, Usukura J, Tano Y, Fujikado T, Furukawa T, Pikachurin, a dystroglycan ligand, is essential for photoreceptor ribbon synapse formation. Nat Neurosci 11, 923–931 (2008); published online EpubAug ([PubMed: 18641643]
17. Orlandi C, Omori Y, Wang Y, Cao Y, Ueno A, Roux MJ, Condomitti G, de Wit J, Kanagawa M, Furukawa T, Martemyanov KA, Transsynaptic Binding of Orphan Receptor GPR179 to Dystroglycan-Pikachurin Complex Is Essential for the Synaptic Organization of Photoreceptors. Cell Rep 25, 130–145 e135 (2018); published online EpubOct 2 (10.1016/j.celrep.2018.08.068). [PubMed: 30282023]
18. Lee Y, Kameya S, Cox GA, Hsu J, Hicks W, Maddatu TP, Smith RS, Naggert JK, Peachey NS, Nishina PM, Ocular abnormalities in Large(myd) and Large(vls) mice, spontaneous models for muscle, eye, and brain diseases. Molecular and cellular neurosciences 30, 160–172 (2005); published online EpubOct (10.1016/j.mcn.2005.07.009). [PubMed: 16111892]
19. Patil DN, Singh S, Laboute T, Strutzenberg TS, Qiu X, Wu D, Novick SJ, Robinson CV, Griffin PR, Hunt JF, Izard T, Singh AK, Martemyanov KA, Cryo-EM structure of human GPR158 receptor coupled to the RGS7-Gβ5 signaling complex. Science 375, p86–91 (2022).
20. Vizurraga A, Adhikari R, Yeung J, Yu M, Tall GG, Mechanisms of adhesion G protein-coupled receptor activation. J Biol Chem 295, 14065–14083 (2020); published online EpubOct 9 (10.1074/jbc.REV120.007423). [PubMed: 32763969]
21. Dunn HA, Orlandi C, Martemyanov KA, Beyond the Ligand: Extracellular and Transcellular G Protein-Coupled Receptor Complexes in Physiology and Pharmacology. Pharmacol Rev 71, 503–519 (2019); published online EpubOct (10.1124/pr.119.018044). [PubMed: 31515243]
22. Cao Y, Sarria I, Fehlhaber KE, Kamasawa N, Orlandi C, James KN, Hazen JL, Gardner MR, Farzan M, Lee A, Baker S, Baldwin K, Sampath AP, Martemyanov KA, Mechanism for Selective Synaptic Wiring of Rod Photoreceptors into the Retinal Circuitry and Its Role in Vision. Neuron 87, 1248–1260 (2015); published online EpubSep 23 (10.1016/j.neuron.2015.09.002). [PubMed: 26402607]
23. Tomioka NH, Yasuda H, Miyamoto H, Hatayama M, Morimura N, Matsumoto Y, Suzuki T, Odagawa M, Odaka YS, Iwayama Y, Won Um J, Ko J, Inoue Y, Kaneko S, Hirose S, Yamada K, Yoshikawa T, Yamakawa K, Aruga J, Elfn1 recruits presynaptic mGluR7 in trans and its loss results in seizures. Nat Commun 5, 4501 (2014)10.1038/ncomms5501). [PubMed: 25047565]
24. Um JW, Kaufman AC, Kostylev M, Heiss JK, Stagi M, Takahashi H, Kerrisk ME, Vortmeyer A, Wisniewski T, Koleske AJ, Gunther EC, Nygaard HB, Strittmatter SM, Metabotropic glutamate receptor 5 is a coreceptor for Alzheimer abeta oligomer bound to cellular prion protein. Neuron 79, 887–902 (2013); published online EpubSep 4 (10.1016/j.neuron.2013.06.036). [PubMed: 24012003]
25. Rice HC, de Malmazet D, Schreurs A, Frere S, Van Molle I, Volkov AN, Creemers E, Vertkin I, Nys J, Ranaivoson FM, Comoletti D, Savas JN, Remaut H, Balschun D, Wierda KD, Slutsky I, Farrow K, De Strooper B, de Wit J, Secreted amyloid-beta precursor protein functions as a GABABR1a ligand to modulate synaptic transmission. Science 363, (2019); published online EpubJan 11 (10.1126/science.aao4827).
26. Orlandi C, Posokhova E, Masuho I, Ray TA, Hasan N, Gregg RG, Martemyanov KA, GPR158/179 regulate G protein signaling by controlling localization and activity of the RGS7 complexes. J Cell Biol 197, 711–719 (2012); published online EpubJun 11 (10.1083/jcb.201202123). [PubMed: 22689652]
27. Anantharaman V, Aravind L, Cache - a signaling domain common to animal Ca(2+)-channel subunits and a class of prokaryotic chemotaxis receptors. Trends Biochem Sci 25, 535–537 (2000); published online EpubNov (10.1016/s0968-0004(00)01672-8). [PubMed: 11084361]

28. Laboute T, Zucca S, Holcomb M, Patil DN, Garza C, Wheatley BA, Roy RN, Forli S, Martemyanov KA, Orphan receptor GPR158 serves as a metabotropic glycine receptor: mGlyR. Science 379, 1352–1358 (2023); published online EpubMar 31 (10.1126/science.add7150). [PubMed: 36996198]

29. Orhan E, Prezeau L, El Shamieh S, Bujakowska KM, Michiels C, Zagar Y, Vol C, Bhattacharya SS, Sahel JA, Sennlaub F, Audo I, Zeitz C, Further insights into GPR179: expression, localization, and associated pathogenic mechanisms leading to complete congenital stationary night blindness. Invest Ophthalmol Vis Sci 54, 8041–8050 (2013); published online EpubDec 9 (10.1167/iovs.13-12610). [PubMed: 24222301]

30. Goehring A, Lee CH, Wang KH, Michel JC, Claxton DP, Baconguis I, Althoff T, Fischer S, Garcia KC, Gouaux E, Screening and large-scale expression of membrane proteins in mammalian cells for structural studies. Nat Protoc 9, 2574–2585 (2014); published online EpubNov (10.1038/nprot.2014.173). [PubMed: 25299155]

31. Faravelli S, Campioni M, Palamini M, Canciani A, Chiapparino A, Forneris F, Optimized Recombinant Production of Secreted Proteins Using Human Embryonic Kidney (HEK293) Cells Grown in Suspension. Bio Protoc 11, e3998 (2021); published online EpubApr 20 (10.21769/BioProtoc.3998).

32. Kabsch W, Xds. Acta Crystallogr D Biol Crystallogr 66, 125–132 (2010); published online EpubFeb (10.1107/S0907444909047337). [PubMed: 20124692]

33. Evans PR, Murshudov GN, How good are my data and what is the resolution? Acta Crystallogr D Biol Crystallogr 69, 1204–1214 (2013); published online EpubJul (10.1107/S0907444913000061). [PubMed: 23793146]

34. McCoy AJ, Grosse-Kunstleve RW, Adams PD, Winn MD, Storoni LC, Read RJ, Phaser crystallographic software. J Appl Crystallogr 40, 658–674 (2007); published online EpubAug 1 (10.1107/S0021889807021206). [PubMed: 19461840]

35. Pernigo S, Fukuzawa A, Beedle AEM, Holt M, Round A, Pandini A, Garcia-Manyes S, Gautel M, Steiner RA, Binding of Myomesin to Obscurin-Like-1 at the Muscle M-Band Provides a Strategy for Isoform-Specific Mechanical Protection. Structure 25, 107–120 (2017); published online EpubJan 3 (10.1016/j.str.2016.11.015). [PubMed: 27989621]

36. Le BV, Kim H, Choi J, Kim JH, Hahn MJ, Lee C, Kim KK, Hwang HY, Crystal structure of the LG3 domain of endorepellin, an angiogenesis inhibitor. J Mol Biol 414, 231–242 (2011); published online EpubNov 25 (10.1016/j.jmb.2011.09.048). [PubMed: 21996443]

37. Terwilliger TC, Grosse-Kunstleve RW, Afonine PV, Moriarty NW, Zwart PH, Hung LW, Read RJ, Adams PD, Iterative model building, structure refinement and density modification with the PHENIX AutoBuild wizard. Acta Crystallogr D Biol Crystallogr 64, 61–69 (2008); published online EpubJan (10.1107/S090744490705024X). [PubMed: 18094468]

38. Chojnowski G, Choudhury K, Heuser P, Sobolev E, Pereira J, Oezugurel U, Lamzin VS, The use of local structural similarity of distant homologues for crystallographic model building from a molecular-replacement solution. Acta Crystallogr D Struct Biol 76, 248–260 (2020); published online EpubMar 1 (10.1107/S2059798320000455). [PubMed: 32133989]

39. Emsley P, Lohkamp B, Scott WG, Cowtan K, Features and development of Coot. Acta Crystallogr D Biol Crystallogr 66, 486–501 (2010); published online EpubApr (10.1107/S0907444910007493). [PubMed: 20383002]

40. Adams PD, Afonine PV, Bunkoczi G, Chen VB, Davis IW, Echols N, Headd JJ, Hung LW, Kapral GJ, Grosse-Kunstleve RW, McCoy AJ, Moriarty NW, Oeffner R, Read RJ, Richardson DC, Richardson JS, Terwilliger TC, Zwart PH, PHENIX: a comprehensive Python-based system for macromolecular structure solution. Acta Crystallogr D Biol Crystallogr 66, 213–221 (2010); published online EpubFeb (10.1107/S0907444909052925). [PubMed: 20124702]

41. Gore S, Sanz Garcia E, Hendrickx PMS, Gutmanas A, Westbrook JD, Yang H, Feng Z, Baskaran K, Berrisford JM, Hudson BP, Ikegawa Y, Kobayashi N, Lawson CL, Mading S, Mak L, Mukhopadhyay A, Oldfield TJ, Patwardhan A, Peisach E, Sahni G, Sekharan MR, Sen S, Shao C, Smart OS, Ulrich EL, Yamashita R, Quesada M, Young JY, Nakamura H, Markley JL, Berman HM, Burley SK, Velankar S, Kleywegt GJ, Validation of Structures in the Protein Data Bank. Structure 25, 1916–1927 (2017); published online EpubDec 5 (10.1016/j.str.2017.10.009). [PubMed: 29174494]

42. Scheres SH, RELION: implementation of a Bayesian approach to cryo-EM structure determination. J Struct Biol 180, 519–530 (2012); published online EpubDec (10.1016/j.jsb.2012.09.006). [PubMed: 23000701]
43. Punjani A, Rubinstein JL, Fleet DJ, Brubaker MA, cryoSPARC: algorithms for rapid unsupervised cryo-EM structure determination. Nat Methods 14, 290–296 (2017); published online EpubMar (10.1038/nmeth.4169). [PubMed: 28165473]
44. Zheng SQ, Palovcak E, Armache JP, Verba KA, Cheng Y, Agard DA, MotionCor2: anisotropic correction of beam-induced motion for improved cryo-electron microscopy. Nat Methods 14, 331–332 (2017); published online EpubApr (10.1038/nmeth.4193). [PubMed: 28250466]
45. Bepler T, Kelley K, Noble AJ, Berger B, Topaz-Denoise: general deep denoising models for cryoEM and cryoET. Nat Commun 11, 5208 (2020); published online EpubOct 15 (10.1038/s41467-020-18952-1). [PubMed: 33060581]
46. Pettersen EF, Goddard TD, Huang CC, Couch GS, Greenblatt DM, Meng EC, Ferrin TE, UCSF Chimera--a visualization system for exploratory research and analysis. J Comput Chem 25, 1605–1612 (2004); published online EpubOct (10.1002/jcc.20084). [PubMed: 15264254]
47. Emsley P, Cowtan K, Coot: model-building tools for molecular graphics. Acta Crystallogr D Biol Crystallogr 60, 2126–2132 (2004); published online EpubDec (10.1107/S0907444904019158). [PubMed: 15572765]
48. Afonine PV, Grosse-Kunstleve RW, Echols N, Headd JJ, Moriarty NW, Mustyakimov M, Terwilliger TC, Urzhumtsev A, Zwart PH, Adams PD, Towards automated crystallographic structure refinement with phenix.refine. Acta Crystallogr D Biol Crystallogr 68, 352–367 (2012); published online EpubApr (10.1107/S0907444912001308). [PubMed: 22505256]
49. Pettersen EF, Goddard TD, Huang CC, Meng EC, Couch GS, Croll TI, Morris JH, Ferrin TE, UCSF ChimeraX: Structure visualization for researchers, educators, and developers. Protein Sci 30, 70–82 (2021); published online EpubJan (10.1002/pro.3943). [PubMed: 32881101]
50. Panjkovich A, Svergun DI, CHROMIXS: automatic and interactive analysis of chromatography-coupled small-angle X-ray scattering data. Bioinformatics 34, 1944–1946 (2018); published online EpubJun 1 (10.1093/bioinformatics/btx846). [PubMed: 29300836]
51. Konarev VVVPV, Sokolova AV, Koch MHJ and Svergun DI, PRIMUS: a Windows PC-based system for small-angle scattering data analysis. J. Appl. Cryst 36, 1277–1282 (2003)10.1107/S0021889803012779).
52. D. I. S, Determination of the regularization parameter in indirect-transform methods using perceptual criteria. J. Appl. Cryst 25, 495–503 (1992)10.1107/S0021889892001663).
53. Svergun DI, Petoukhov MV, Koch MH, Determination of domain structure of proteins from X-ray solution scattering. Biophys J 80, 2946–2953 (2001); published online EpubJun (10.1016/S0006-3495(01)76260-1). [PubMed: 11371467]
54. V. V. V a. D. I. S, Uniqueness of ab initio shape determination in small-angle scattering. J. Appl. Cryst 36, 860–864 (2003)10.1107/S0021889803000268).
55. Panjkovich A, Svergun DI, SASpy: a PyMOL plugin for manipulation and refinement of hybrid models against small angle X-ray scattering data. Bioinformatics 32, 2062–2064 (2016); published online EpubJul 1 (10.1093/bioinformatics/btw071). [PubMed: 27153695]
56. Chalmers MJ, Busby SA, Pascal BD, He Y, Hendrickson CL, Marshall AG, Griffin PR, Probing protein ligand interactions by automated hydrogen/deuterium exchange mass spectrometry. Anal Chem 78, 1005–1014 (2006); published online EpubFeb 15 (10.1021/ac051294f). [PubMed: 16478090]
57. Zhang Z, Smith DL, Determination of amide hydrogen exchange by mass spectrometry: a new tool for protein structure elucidation. Protein Sci 2, 522–531 (1993); published online EpubApr (10.1002/pro.5560020404). [PubMed: 8390883]
58. Pascal BD, Willis S, Lauer JL, Landgraf RR, West GM, Marciano D, Novick S, Goswami D, Chalmers MJ, Griffin PR, HDX workbench: software for the analysis of H/D exchange MS data. J Am Soc Mass Spectrom 23, 1512–1521 (2012); published online EpubSep (10.1007/s13361-012-0419-6). [PubMed: 22692830]
59. Keppel TR, Weis DD, Mapping residual structure in intrinsically disordered proteins at residue resolution using millisecond hydrogen/deuterium exchange and residue averaging. J Am Soc

Mass Spectrom 26, 547–554 (2015); published online EpubApr (10.1007/s13361-014-1033-6). [PubMed: 25481641]

60. Masuho I, Martemyanov KA, Lambert NA, Monitoring G Protein Activation in Cells with BRET. Methods Mol Biol 1335, 107–113 (2015)10.1007/978-1-4939-2914-6_8). [PubMed: 26260597]

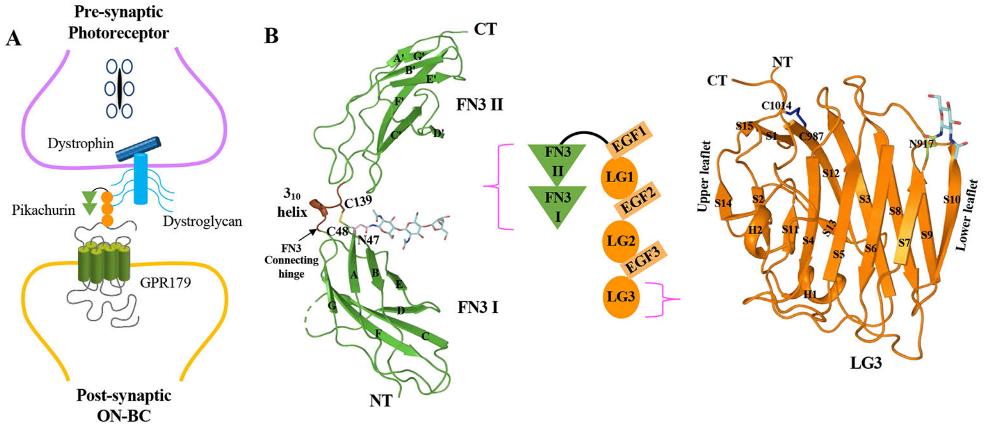

Fig. 1. Role of pikachurin in photoreceptor synapse organization and crystal structures of the constituent domains of pikachurin.

(**A**) pikachurin forms a transsynaptic connection by interacting with the pre-synaptic photoreceptor dystroglycan complex (DGC) and the post-synaptic receptor GPR179 at the ON-bipolar cell (ON-BC). (**B**) pikachurin is composed of an N-terminal FN3 tandem followed by three EGF-LG tandems (middle). Left: A cartoon representation of the crystal structure of the N-terminal FN3 tandem is shown in green. The FN3 connecting loop harboring the 3_{10} helix and disulfide bridge provides rigidity to the bent FN3 tandem assembly. Glycosylation at Asn^{47} (N47) is shown with cyan-colored carbohydrate moieties. Right: The crystal structure of the C-terminal LG3 domain is represented in orange. Glycosylation and disulfide bridge sites are shown in cyan and blue, respectively. CT, C terminus; NT, N terminus.

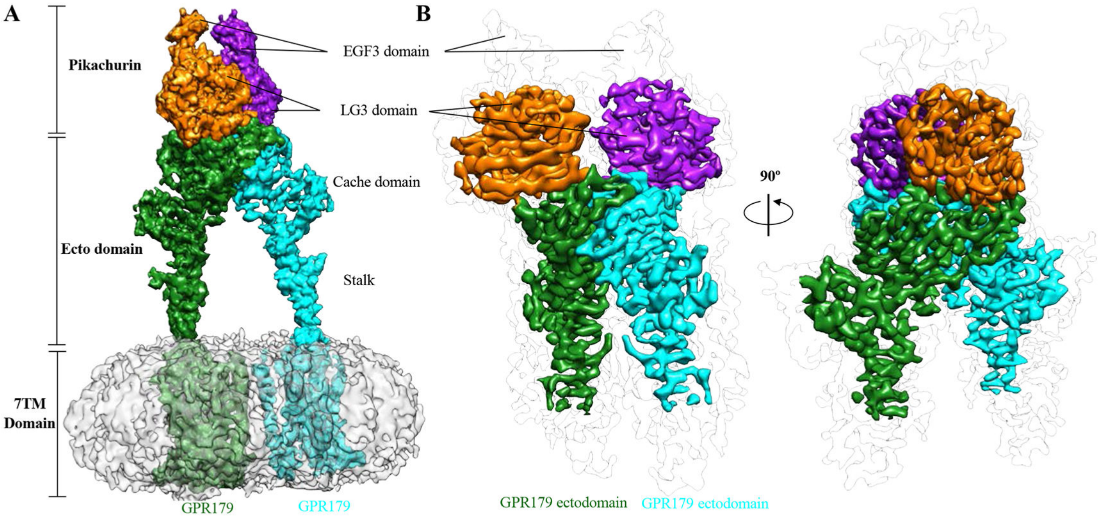

Fig. 2. Cryo-EM structure of pikachurin complexed with GPR179.

(**A**) Cryo-EM map of a GPR179 homodimer complexed with the EGF3-LG3 of pikachurin. GPR179 protomers are shown in cyan and green, whereas the pikachurin domains are shown in orange and purple. (**B**) Focused refinement of the GPR179 ectodomains and the pikachurin domains provides well-resolved density for the GPR179 dimeric Cache domain and the LG3 domains. Regions with poor density were excluded from the final model.

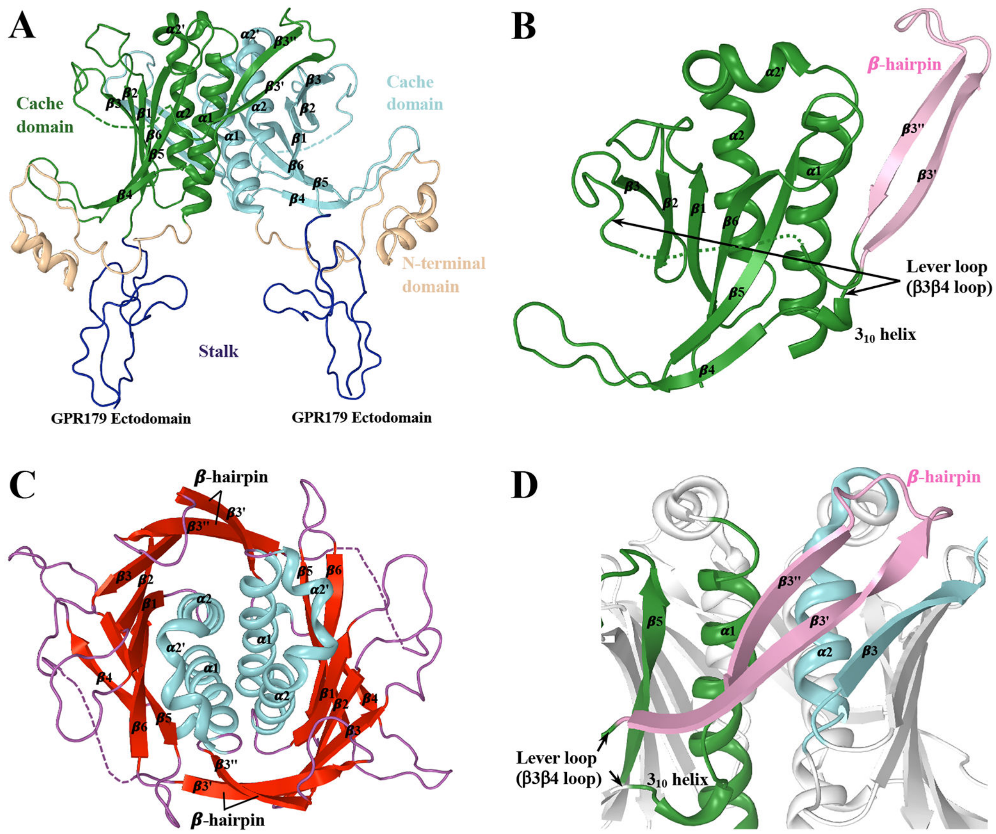

Fig. 3. Structural organization of the GPR179 ectodomain featuring the Cache domain.

(**A**) The GPR179 ectodomain is composed of an N-terminal domain, a Cache domain, and a stalk region. Its dimeric assembly through the Cache domain is shown as a side view in the cartoon representation. (**B**) GPR179 contains a central globular domain, a Cache domain that is composed of six antiparallel β-sheets bordered by α-helices from the backside and a β-hairpin in the lever loop. (**C**) Top view of Cache domain dimerization, which generates a β-barrel–like shape that captures α-helices at the barrel pore. The β-hairpin fills the gap between the two antiparallel β-sheets cores of the Cache domains at the dimeric interface resembling the barrel fold. (**D**) The β-hairpin is also involved in the dimeric interface, interacting with the α2 and β3 residues of another Cache domain (shown in cyan).

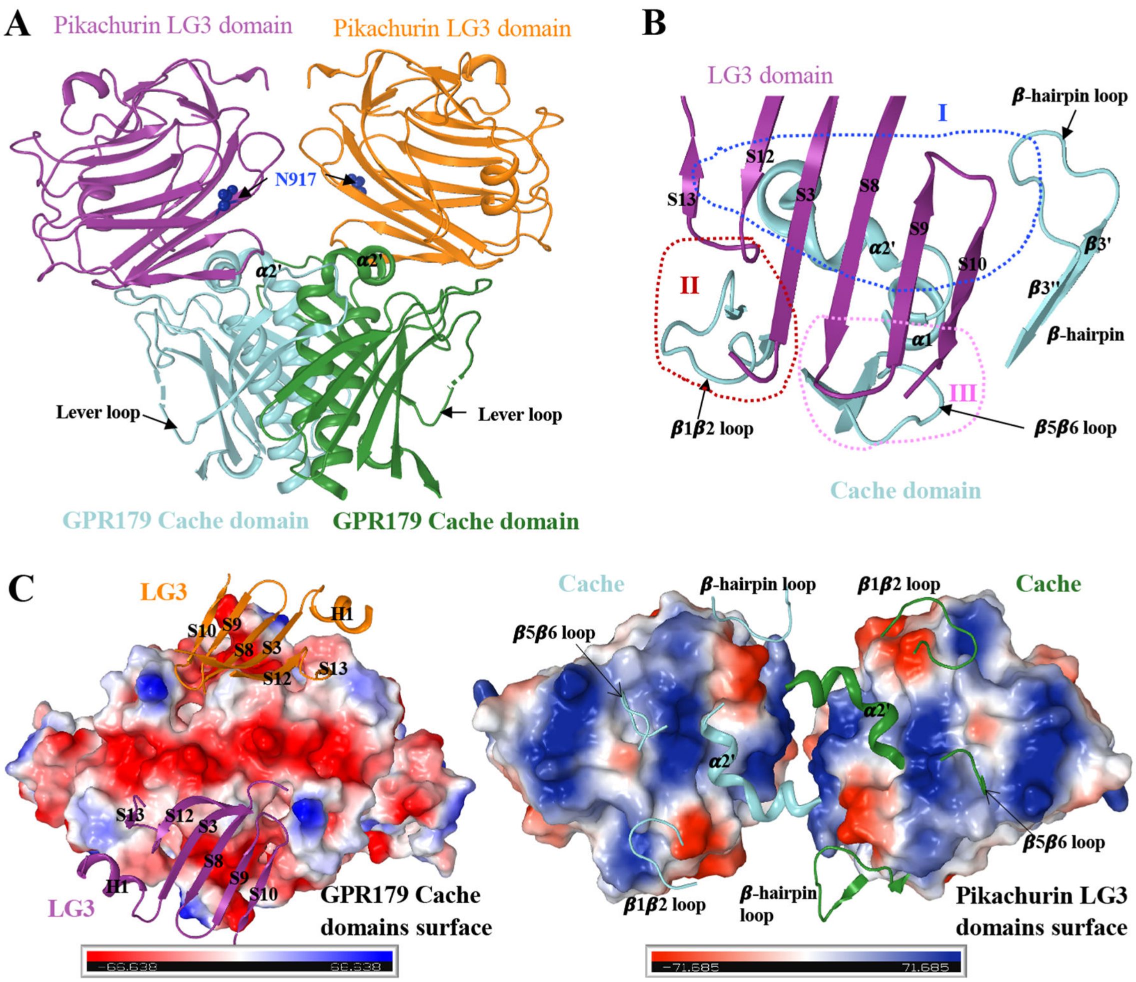

Fig. 4. Mechanism of interaction between pikachurin and GPR179.

(**A**) Cartoon representation of overall interaction between the Cache domains of GPR179 and the LG3 domains of pikachurin, in which each Cache domain mainly targets one LG3 domain, forming a tetrameric assembly. The glycosylation site at Asn^{917} (N917, blue sphere) is distant from the interaction interface. (**B**) Binding site I involves the lower leaflet of the β-sandwich core of LG3, which passes perpendicularly over the α-helix α2' and the β-hairpin at the top of the Cache domain. Sites II and III stabilize the binding at opposing ends involving loop regions. (**C**) Maps of surface electrostatic potentials. The binding of pikachurin generates a complementary electrostatic surface for favorable complex formation with GPR179.

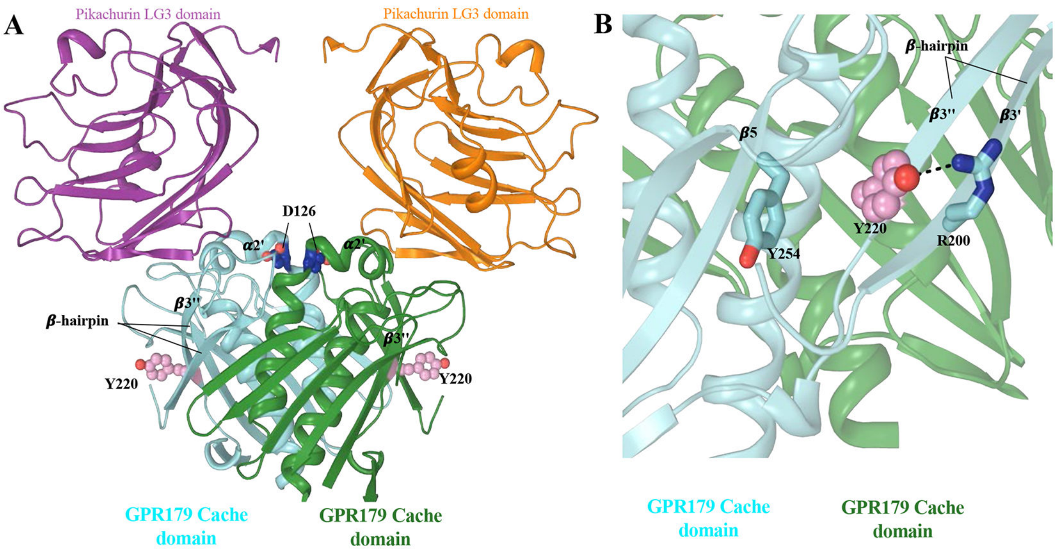

Fig. 5. Analysis of the effects of CSNB-associated mutations on GPR179 structure.

(**A**) The mutations D126H and Y220C are found in the Cache domain of GPR179 (represented as sticks). Asp^{126} (D126, blue) is present in the α2' helix, whereas Tyr^{220} (Y220) is located in the β3'' β-hairpin sheet and can participate in stabilization of GPR179 homodimeric assembly. (**B**) Tyr^{220} (Y220) can form a π-π interaction with Tyr^{254} (Y254) of the β5 strand and participate in hydrogen bonding with Arg^{200} (R200) of β3'.0 The Y220C mutation would be expected to hamper these interactions, ultimately destabilizing the dimeric interface involving the β-hairpin.